crystals

MDPI

Article

Effect of Laser Energy Density on the Microstructure and Microhardness of Inconel 718 Alloy Fabricated by Selective Laser Melting

Jing Xu [1,†], Zichun Wu [1,†], Jianpeng Niu [1], Yufeng Song [1], Chaoping Liang [2], Kai Yang [3,4], Yuqiang Chen [1] and Yang Liu [1,2,4,*]

1 Hunan Engineering Research Center of Forming Technology and Damage Resistance Evaluation for High Efficiency Light Alloy Components, Hunan University of Science and Technology, Xiangtan 411201, China
2 National Key Laboratory of Science and Technology on High-Strength Structural Materials, Central South University, Changsha 410083, China
3 College of Engineering, Peking University, Beijing 100871, China
4 Hunan Vanguard Group Co., Ltd., Changsha 410100, China
* Correspondence: liuyang7740038@163.com
† These authors contributed equally to this work.

Abstract: This work focused on the effects of laser energy density on the relative density, microstructure, and microhardness of Inconel 718 alloy manufactured by selective laser melting (SLM). The microstructural architectures, element segregation behavior in the interdendritic region and the evolution of laves phases of the as-SLMed IN718 samples were analyzed by optical metallography (OM), scanning electron microscopy (SEM), energy dispersive spectrometer (EDS), and electron probe microanalysis (EPMA). The results show that with an increase in the laser volume energy density, the relative density and the microhardness firstly increased and then decreased slightly. It also facilitates the precipitation of Laves phase. The variation of mechanical properties of the alloy can be related to the densification degree, microstructure uniformity, and precipitation phase content of Inconel 718 alloy.

Keywords: selective laser melting; Inconel 718 alloy; laser energy density; microstructure; microhardness

Citation: Xu, J.; Wu, Z.; Niu, J.; Song, Y.; Liang, C.; Yang, K.; Chen, Y.; Liu, Y. Effect of Laser Energy Density on the Microstructure and Microhardness of Inconel 718 Alloy Fabricated by Selective Laser Melting. *Crystals* **2022**, *12*, 1243. https://doi.org/10.3390/cryst12091243

Academic Editor: Cyril Cayron

Received: 25 July 2022
Accepted: 30 August 2022
Published: 2 September 2022

1. Introduction

Inconel 718 (IN718), a typical precipitation-strengthened nickel-based superalloy, possesses excellent mechanical properties such as good oxidation resistance, good weldability, corrosion resistance, high creep resistance, and high fatigue strength at high temperatures [1–4]. It has been widely used in high-temperature components such as turbine disks, aerospace gas turbine blades, and combustion chambers [5–8]. However, forging and casting, as the conventional manufacturing processes for IN718 alloy, are difficult for producing complex integral structures, owing to high density, high melting point, and severe work hardening [9–11]. Moreover, the higher cost of the traditional machining methods, which are laborious and time-consuming, leads to a sharp increase in production cost [5,12]. The emergence of additive manufacturing provides a feasible way to overcome these disadvantages, which can help reduce material waste to a bare minimum and to reduce production time for complex parts [13].

Selective laser melting (SLM) has advantages such as high forming precision [14] and integrated forming of high mechanical properties complex components [15], so it has become one of the most promising additive manufacturing technologies for metallic materials [4,16–18]. Due to the rapid cooling rate of the molten pool in the SLM process [19], near net shape products with fine microstructure and excellent metallurgical strength can be manufactured layer by layer, such as complex parts manufactured with titanium alloy [20–22], steel [23,24], superalloys [25,26], and other materials [27–29].

Currently, many researchers have carried out research on the microstructure and properties of IN718 by means of SLM, hoping to regulate the microstructure and properties by adjusting the processing parameters, such as laser power, scanning speed, and scanning strategies, hatch spacing, and so on. For example, Wang et al. [30] found that the grain refinement caused by an increase in scanning speed further weakens the anisotropy of mechanical properties, which is conducive to obtaining a more homogenous microstructure and a higher production rate for SLM manufacturing. Pan et al. [31] investigated the independent effects of laser power and scanning speed of SLM on the precipitation and mechanical properties of identically heat-treated IN718 alloys. Liu et al. [32] studied the effects of two scanning strategies (single-directional scanning and cross-directional scanning) on the solidification structure and crystallographic texture of SLM-manufactured IN718 alloy. Ravichander et al. [33] identified the effect of scan strategy on residual stress and studied the metallurgical interactions between the mechanical and microstructural properties within the IN718 superalloy. Wang et al. [34] optimized the process parameters for selective laser melting of Inconel 718 and further established the relationship equation between the relative density of SLMed samples and the energy density coupled by laser parameters. Zhu et al. [35] reported that fine and coarse columnar dendritic microstructure of as-deposited IN718 superalloy were, respectively, obtained at different laser power and laser beam diameter and found that the Nb- and Mo-rich Laves phase is formed in the interdendritic regions, which weakens the mechanical property of the as-deposited IN718 superalloy [8,36–38]. Ma [39] pointed out that with increasing energy input, there was a dendrite-to-cell transition in the dendritic morphology evolution of the as-DLFed IN718 samples; in addition, the size and volume fraction of the Laves phase at the boundary between dendrites increased. However, although the laser parameters have been found to affect the precipitation of IN718 alloy, and the laser energy density was confirmed to control the microstructure and mechanical properties of SLM-manufactured Inconel 718 alloy, the relation between the laser energy density, microstructure, and properties has yet been thoroughly investigated.

Therefore, in this paper, Inconel 718 samples were fabricated by selective laser melting, and the effect of laser energy density on relative density was discussed. The microstructural architectures, the element segregation behavior in the interdendritic region, the evolution of the Laves phases with different volume energy density SLMed IN718 samples were analyzed. The microhardness of the samples was also measured to further clarify the mechanical response to the microstructure evolution of the samples at different volume energy densities. The aim of this study is to provide an insight into the effects of laser energy density on the microstructure and microhardness of the as-SLMed IN718 alloys.

2. Materials and Methods

2.1. Materials and Experimental Equipment

The gas-atomized commercially available Inconel 718 powder (Avimetal Powder Metallurgy Technology Co., Ltd., Beijing, China) was used for the present study. The morphology of Inconel 718 powder was characterized by scanning electron microscope (Nova Nano SEM230, FEI Co., Ltd., Hillsboro, OR, USA). The size distribution of Inconel 718 powders was measured using a laser particle size analyzer (Mastersizer 3000) (Malvery Instruments Ltd., Malvern, UK). The chemical composition of Inconel 718 powder was determined by inductively coupled plasma atomic emission spectrometer (ICP-AES) (Thermo Fisher Scientific Co., Ltd., Waltham, MA, USA). The morphologies and size distributions of the Inconel 718 powders are presented in Figure 1. The powder particles are spherical shape with the size of 15–53 μm. The D10, D50, and D90 of Inconel 718 powders were 19.86 μm, 29.56 μm, and 39.42 μm, respectively. The chemical composition of Inconel 718 powder is listed in Table 1. The SLM experiment was carried out by an DiMetal-100 3D printing machine equipped with a 200 W Yb-fiber laser beam (Guangzhou Lejia Additive Technology Co., Ltd., Guangzhou, China). Prior to the selective laser melting process, the powder was dried in vacuum-drying oven at the temperature of 60 °C for 4 h, to reduce the residual oxygen content and the humidity. During the manufacturing process, argon gas (99.99% purity) was filled in the working chamber with oxygen maintained below 50 ppm, which is conducive to prevent the powder and melt pool from oxidizing during SLM processing.

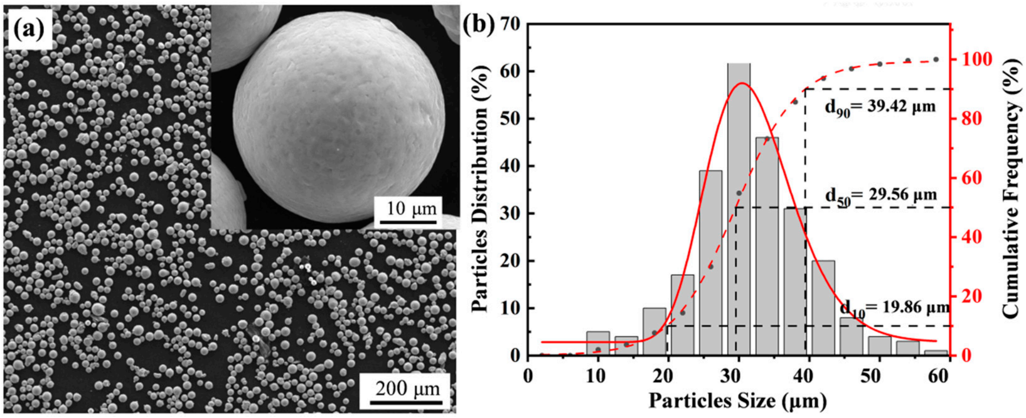

Figure 1. Morphology (**a**) and size distribution (**b**) of Inconel 718 powder.

Table 1. Chemical composition (wt. %) of the Inconel 718 powder.

Elements	Ni	Cr	Nb	Mo	Ti	Al	Co	Fe
Inconel 718	51.13	19.34	5.14	3.04	0.93	0.58	0.03	Balanced

2.2. Sample Fabrications and Characterization

The Taguchi method was used to optimize the parameters for the SLM Inconel 718 alloy in this study. The experiments were conducted with three controllable five-level process parameters: laser power, scanning speed, and scanning interval. The process parameters and their levels are given in Table 2. The design of experiments based on L25 orthogonal array was obtained, as shown in Table 3, using MINITAB statistical software (version 16). A series of samples with 20 mm × 20 mm × 20 mm cubes were prepared at above-mentioned different laser energy density by varying laser power, scanning speed, and scanning interval. The experimental results and associated processing parameter of SLM-fabricated Inconel 718 alloy process, according to L25 orthogonal array, are shown in Table 3.

After SLM fabrication, the as-SLMed Inconel 718 alloy samples were cut parallel and perpendicular to the building direction of the sample using wire electric discharge machining. The specimens were polished by 2000 grit SiC paper and etched in a solution of 10 mL HCl + 3 mL H_2O_2 for 20 s. The microstructure of the as-SLMed Inconel 718 alloy samples was characterized by optical microscope (Olympus BX51 M) (Olympus Co., Ltd., Tokyo, Japan) and scanning electron microscope (Nova Nano SEM230) (FEI Co., Ltd., Hillsboro, OR, USA) using back-scattered mode (SEM-BSE) (FEI Co., Ltd., Hillsboro, OR, USA). The element segregation and Laves phase elemental distribution were analyzed by electron probe microanalysis (EPMA, JXA8530F) (Japan Electronics Co., Ltd., Tokyo, Japan).

Table 2. The process parameters and their levers used in this study.

Parameters	Level 1	Level 2	Level 3	Level 4	Level 5
A: Laser power (W)	160	170	180	190	200
B: Scanning speed (mm/s)	800	900	1000	1100	1200
C: Scanning interval (mm)	0.06	0.07	0.08	0.09	0.1

Table 3. Experimental design of L25 orthogonal array and experimental results for relative density.

Runs	Laser Power (W)	Scanning Speed (mm/s)	Scanning Interval (mm)	Volume Energy Density (J/mm^3)	Relative Density (%)
1	150	800	0.06	104.17	99.12
2	150	900	0.07	79.37	99.26
3	150	1000	0.08	62.50	96.13
4	150	1100	0.09	50.51	95.43
5	**150**	**1200**	**0.10**	**41.67**	**92.28**
6	160	800	0.07	95.24	99.68
7	160	900	0.08	74.07	98.33
8	160	1000	0.09	59.26	97.55
9	160	1100	0.10	48.48	94.48
10	160	1200	0.06	74.07	98.62
11	170	800	0.08	88.54	99.57
12	170	900	0.09	69.96	98.63
13	170	1000	0.10	56.67	97.43
14	**170**	**1100**	**0.06**	**85.86**	**99.23**
15	170	1200	0.07	67.46	97.55
16	180	800	0.09	83.33	99.15
17	180	900	0.10	66.67	98.02
18	**180**	**1000**	**0.06**	**100**	**99.53**
19	180	1100	0.07	77.92	98.92
20	180	1200	0.08	62.50	98.21
21	190	800	0.10	79.17	98.5
22	**190**	**900**	**0.06**	**117.28**	**98.92**
23	190	1000	0.07	90.48	99.43
24	190	1100	0.08	71.97	97.88
25	190	1200	0.09	58.64	96.84

The relative density of the SLM-fabricated samples was measured using Archimedes principle, and the results were presented as a percentage of the Inconel 718 alloy density (8.24 g/cm^3). In order to reduce the randomness of the measurements, five tests were performed for each sample, and the average of our measurement was used as the value of the relative density. The Vickers microhardness tests were performed on the polished cross section using a digital microhardness instrument with a load of 100 g and a dwell time of 10 s. At least three tests were done for each sample, and the averaged measurement was used as the indicator of the Vickers microhardness.

3. Results and Discussion

3.1. Effect of Laser Energy Density on Relative Density

It is desirable to achieve fully densification in the final part in SLM process, since the retention of a small amount of porosity will severely degrades the mechanical properties [3]. As a result, the output parameter for this Taguchi experiment is chosen to be the relative density in this study. The experimental results and associated processing parameter of LPD process according to L25 orthogonal array were listed in Table 3. For SLM, the scanning speed and laser power are key factors for part forming [21,40]. The response surface graph and contour plot, as shown in Figure 2, were obtained to confirm the interaction effects of laser power and scanning speed on relative density. With a decrease in the scanning speed or an increase in the laser power, the approximate change of relative density first increased and then slightly decreased. The interplay between laser power and scanning speed could be deduced as the determinant factors for the densification process of SLM-fabricated Inconel 718 alloy. This discovery is similar to the features found in other material in the previous studies [41–43].

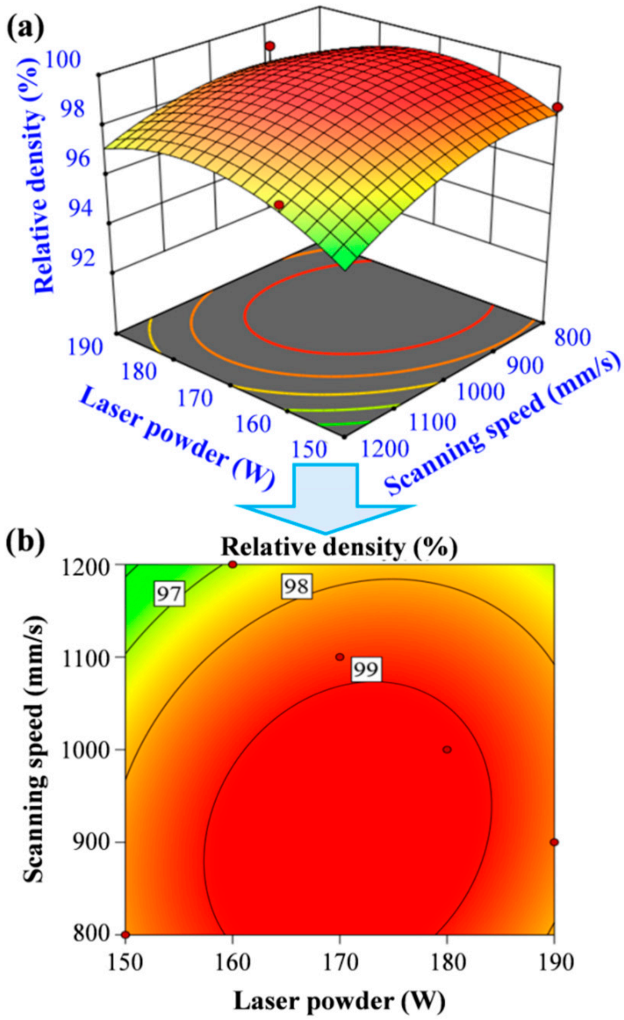

Figure 2. Response surface graph (**a**) and contour plot (**b**) of the effects of laser power and scanning speed on the relative density at scanning interval 0.06 mm.

Volume energy density (E_v) is also a key factor in the densification and significantly affects the microstructure and mechanical properties of SLM-fabricated Inconel 718 alloy [44,45]. The following equation was used to determine the volume energy density (E_v):

$$E_v = \frac{P}{Vht} \tag{1}$$

where P refers to the laser power (W), V is the scanning speed (mm/s), h represents the scanning interval (mm), and t is the powder-bed layer thickness, which kept constant as 0.03 mm. Based on Equation (1), the E_v of each sample are listed in Table 3. In addition, Figure 3 shows the relationship between relative density and volume energy density for the SLM-fabricated Inconel 718 alloy. As can be seen in Figure 3, low energy density (<80 J/mm^3) leads to a low relative density due to the lack of consolidation, while higher energy density is beneficial to the density of SLM-fabricated Inconel 718 alloy. However, when the energy density exceeds approximately 100 J/mm^3, the relative density decreases slightly. This is because the high absorption of heat leads to evaporation of the material. Consequently, gas pores form in the SLMed sample, which can be observed in Figures 4 and 5. Moreover, there is a certain threshold energy density that gives maximum material density in Figure 3. It is approximately 80–110 J/mm^3 for Inconel 718 alloy fabricated by the SLM process, and the relative density can reach more than 99%.

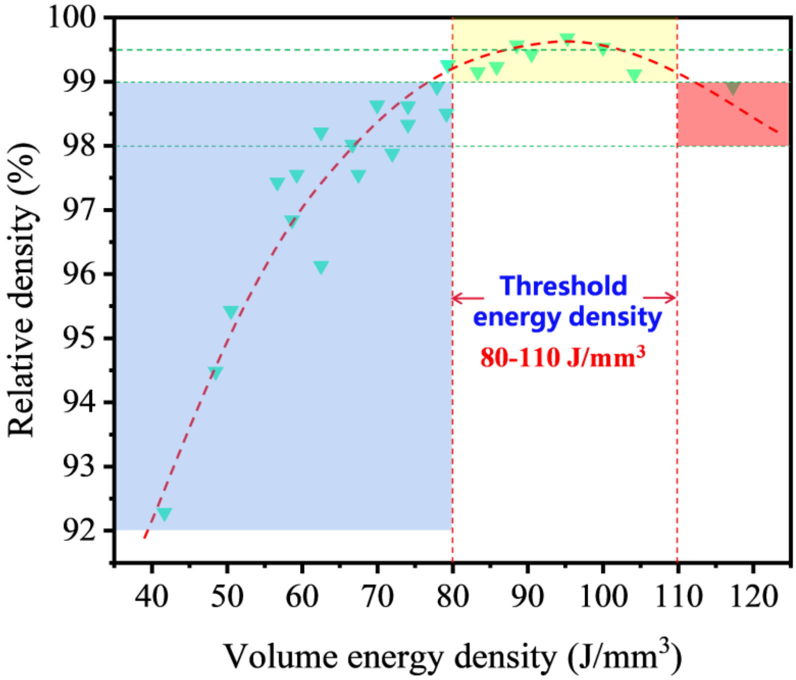

Figure 3. Relationship between relative density and volume energy density for SLM-fabricated Inconel 718 alloy. The points are the results of Table 3.

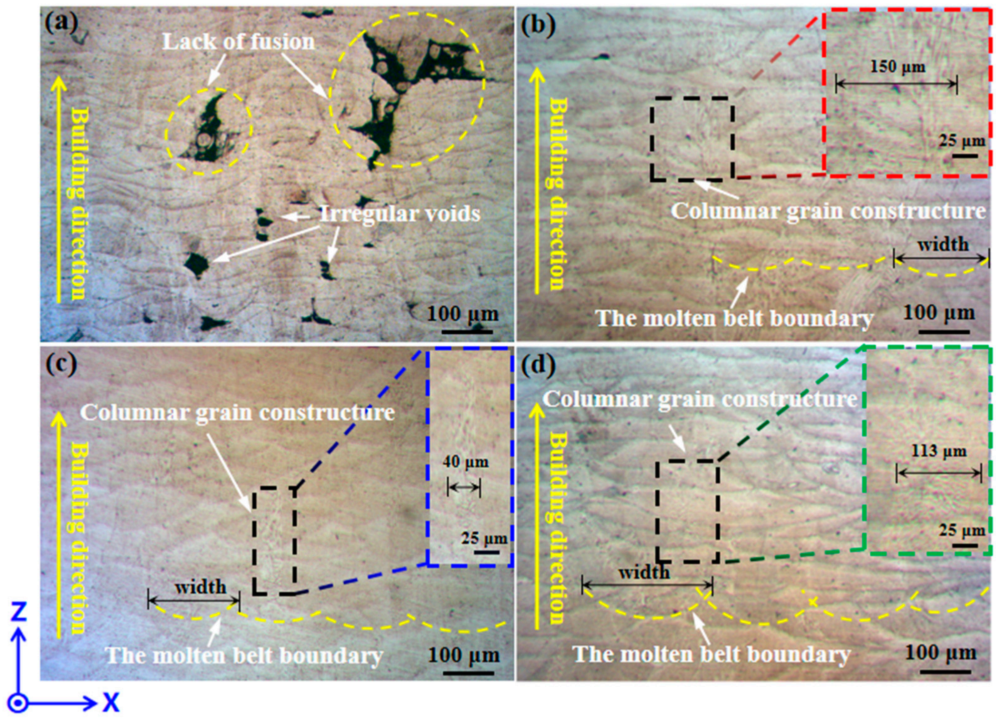

Figure 4. Optical micrographs of the as-SLMed IN718 samples on vertical section (X–Z plane) at the E_vs of (**a**) 41.67 J/mm^3, (**b**) 85.86 J/mm^3, (**c**) 100 J/mm^3, and (**d**) 117.17 J/mm^3.

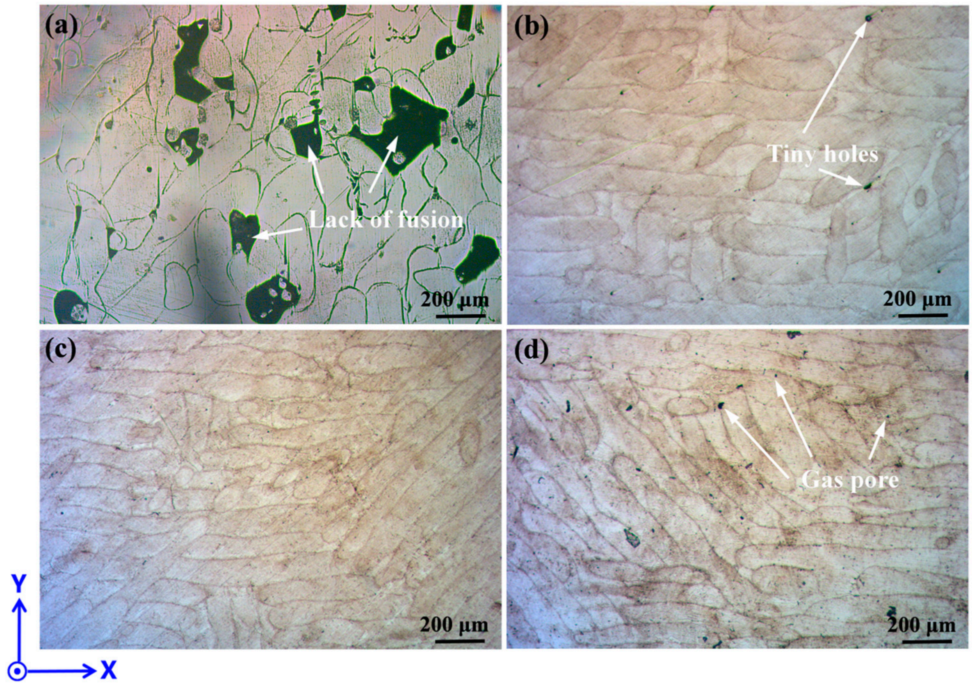

Figure 5. Optical micrographs of the as-SLMed IN718 samples on vertical section (X–Y plane) at the E_v of (**a**) 41.67 J/mm^3, (**b**) 85.86 J/mm3, (**c**) 100 J/mm^3, and (**d**) 117.17 J/mm^3.

3.2. Microstructure Analysis

In this research, four unique samples of #5, #14, #18, and #22, representing different E_v levels, were selected from the above-mentioned 25 samples, for the purpose of clearly explaining the microstructural evolution of as-SLMed Inconel 718 in the following parts. The laser parameters of these four samples selected were marked in bold, as shown in Table 3.

To reveal well the microstructural evolution of all the samples fabricated in this research, the microstructures of these selected four unique samples with different levels of E_v were studied. Figure 4 shows optical micrographs of these four samples on the vertical section (X–Z plane), at E_vs of (a) 41.67 J/mm^3, (b) 85.86 J/mm^3, (c) 100 J/mm^3, and (d) 117.17 J/mm^3, respectively, which could reflect the microstructural architectures of all conditions in this study. The morphologies of the molten pools with the shape of the fish scale and a certain number of pores were observed clearly. It can be seen from Figure 4b–d that increasing energy density from 85.86 to 117.17 J/mm^3 simultaneously increases the width of the molten pool. Figure 4 also shows the change of the characteristics of pores at different E_vs. The shape of the pores changed from irregular shapes with rough boundaries to round shapes with smooth edges as the laser energy density increased from 45.46 to 85.86 J/mm^3. The amount and size of the pores decreased as well. Obviously, the interface was clear and free of pores when the E_v reached 100 J/mm^3. With further increase in E_v, gas pores appeared at the E_v of 117.17 J/mm^3, as shown in Figure 4d.

Figure 4 also indicates the microstructure of the as-SLMed IN718 samples exists with a certain number of columnar grains and dendrites, as circled by the black dashed rectangle. Continuous dendrites, up to even several millimeters in length, grow along the deposition direction and through several melt pools, as shown in the black dashed rectangle. The growth direction of the dendrites is not exactly parallel to the building direction, declining at an angle to the building direction.

The width of the columnar grains ranges from 40 μm to 150 μm. The columnar grains become smooth and fine at the E_v of 100 J/mm^3, while they become coarse and large at E_vs of 85.86 and 117.17 J/mm^3. The interface between two adjacent cladding layers is clear without any change in the columnar grains. For the sample at the E_v of 117.17 J/mm^3, shown in (Figure 4d), the columnar grains are discontinuous. This is believed to be from the different microstructure between the bottom region of the melt pool (planar interface growth) and the other regions (dendrite growth) [46,47].

The microstructures on the X–Y plane of the SLMed samples at different E_vs are shown in Figure 5. A close connection between the densification of the sample and the laser energy density has been found. At the E_v of 41.67 J/mm^3, the insufficient energy input resulted in poor melt pool fluidity and insufficient filling of the inter-particle voids. This causes the appearance of many discrete melt pools. Additionally, a lack of fusion among powders resulted in the formation of large cavities, which were barely recognizable, and some unmelted particles were trapped in the cavities [48]. The large cavities disappeared. Meanwhile, as the laser energy density increased from 45.46 J/mm^3 to 85.86 J/mm^3. Tiny holes were observed in Figure 5b, and unmelted particles were formed. This is due to the fact that some gases were trapped in the melt pool when solidification of the pool occurred, forming small pores [21,49]. When the laser energy density reaches 100 J/mm^3, the melt pool was built up in an orderly manner with good lap from track to layer. As a result, the as-SLMed Inconel 718 alloy was free of pores. Gas pores still occurred as E_v up to 117.17 J/mm^3, as marked with arrows in Figure 5d. Among the three kinds of pores, gas pores are the most in quantity and the minimum in size [46,50]. It should be stressed here that gas pores appear at the laser energy density of 117.17 J/mm^3, which will damage the mechanical properties of sample. We could conclude that increasing properly the E_v benefits the improvement of densification, but an excessive value is undesirable. At a higher E_v, strong interactions between layers may result in high thermal stress and elements evaporation. The appearance of gas pores will eventually damage the mechanical properties of sample.

The observed microstructural differences indicate a tradeoff between the regions processed with low energy density and high energy density, which would improve the mechanical performance.

To further characterize the aforementioned dendritic growth, Figure 6 shows the SEM micrographs that were taken on the X–Z planes of as-SLMed IN718. As exhibited with the yellow dashed lines in Figure 6a, the boundary of molten pool can be visibly indicated after etching. Figure 6b implies that cellular dendrites grown at the boundary of the molten pool opposite the heat flow inclined away from the building direction at a certain angle. This leads to dendrites' growth parallel to the building direction at the center of the molten pool. The columnar dendrites grow in the direction of the heat flow rather than along the build direction. The solidification shifts from the cellular crystals at the bottom of the melt pool to the dendrites above the side of the melt pool. The subcellular tissue in the high energy input region grows into rough cellular crystals, with the appearance of the remelting zone. Another part of the grains near the remelting zone grows into columnar crystals, along the rough interface under the negative temperature gradient. The cellular crystal–dendrite growth is a typical feature of the solidification mode of IN718 during SLM [51].

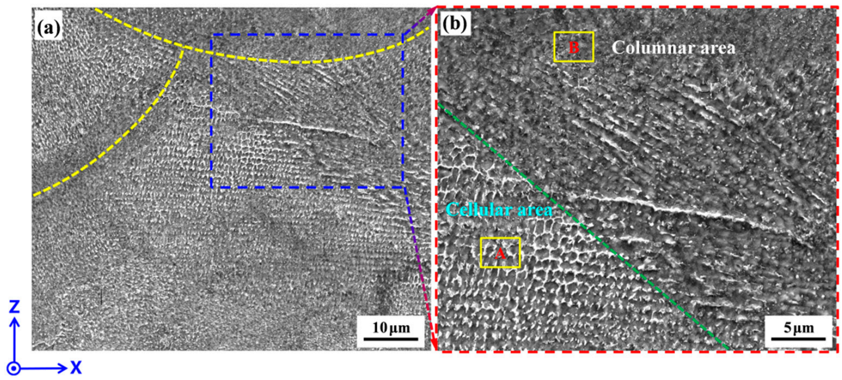

Figure 6. SEM micrographs of the as-built sample in the X–Z plane; (**a**) track–track structures consisting of overlapping area and central fusion area, and (**b**) dendrites and cellular sub-structures contained in the overlapping region.

The element content of the two areas (black matrix and white segregation phase) marked in Figure 6b was analyzed. The dark area (B) was rich in Fe, Cr, and Ni, while the white area (A) was rich in Nb, Mo, and Ti, as indicated in Figure 7 and Table 4. The Laves phase located in the interdendritic regions of the as-SLMed samples was identified [52], This may be a result of segregation during the fast solidification process of the sample via SLM. Recalling the microstructures shown in Figure 6, the microsegregations of Nb and Ti result in the formation of the brittle intermetallic Laves phase. The appearance of the Laves phase will cause a big change in the mechanical properties. For instance, it would affect the mechanical strength of the Inconel 718, making the alloy more brittle and easier to fracture under external force load [37]. The characteristics of the Laves phase are discrepant at different laser energy densities, as shown in Figure 8.

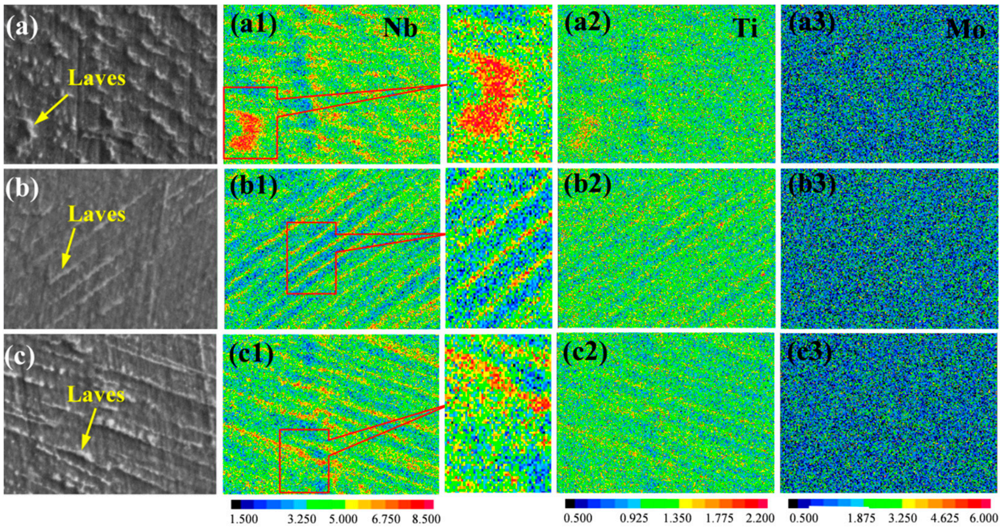

Figure 7. Cross-section EPMA maps of the SLMed Inconel 718 under different volume energy densities, including 85.86 J/mm^3 (**a**–**a3**), 100 J/mm^3 (**b**–**b3**), and 117.17 J/mm^3 (**c**–**c3**).

Table 4. EPMA quantitative analysis results for the position P1 (A) and P2 (B) of Figure 6b.

Element (Wt. %)	Ni	Cr	Fe	Nb	Mo	Ti	Al
White area (A)	48.528	17.681	16.974	7.898	3.175	1.259	0.463
Dark area (B)	49.490	18.714	18.213	5.164	2.882	1.041	0.445

Figure 7 also shows the magnification of the dendrites and the electron probe micro-analysis at different E_vs. It shows the appearance of the Laves phase and the segregation of Nb, Ti, and Mo in the interdendritic region. The Laves phase is lighter yellow, as shown in Figure 7a–c. As the E_v increases from 85.86 J/mm^3 to 100 J/mm^3, the Laves phase becomes less and less obvious. With increasing energy density, the Nb element is less segregated, especially in some interdendritic regions (as shown in the red box). The even distribution of Mo, Nb, and Ti in the crystal and grain boundaries is observed at an energy density of 100 J/mm^3. This indicates that a higher energy density leads to the uniform diffusion of the elements, causing the decrease in the Laves phase. Moreover, the volume fraction of the Laves phase and Nb segregation strongly depend on the solidification processes [35]. The faster cooling rate at a higher energy density greatly improves the dendrite growth rate and solute trapping, so that Nb does not have enough time to diffuse from the solid phase to the liquid phase. This allows more Nb elements to be trapped in the solid phase (matrix), while fewer Nb elements are segregated to structure the Laves phase. However, when the energy density exceeds a critical value, the resulting Nb segregation increases again. The increase in energy density in turn facilitates the precipitation of the Laves phase in Inconel 718 prepared by SLM.

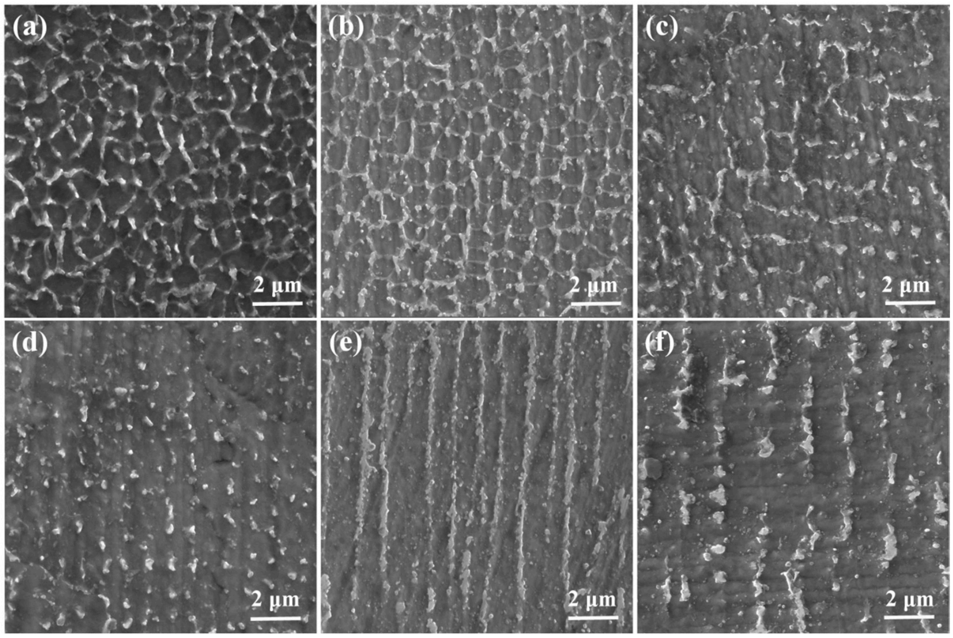

Figure 8. High-magnification SEM graphs of cellular dendrites and columnar dendrites in the X–Z plane of SLMed IN718 samples with different laser volume energy densities; (**a**,**d**) 85.86 J/mm^3, (**b**,**e**) 100 J/mm^3, and (**c**,**f**) 117.17 J/mm^3.

It is known that segregation is a phenomenon largely dependent on time. As a result, it has a tight connection with the cooling rate [35]. Due to the non-equilibrium fast solidification conditions that prevail during SLM, the appearance of the Laves phase easily occurs in as-SLMed IN718 alloy, through the segregation of high atomic diameter elements such as Nb, Mo, and Ti. Accordingly, the Laves phase is easier to appear in the interdendritic boundaries at a low energy density or high energy density. In summary, the proper increase in the volume energy density helps to reduce the precipitation of the Laves phase, while excessive energy will facilitate the formation of the Laves phase in the SLM-fabricated Inconel 718.

To further reveal the influence of volume energy density (E_v) on the microstructures of SLM-processed Inconel 718, Figure 8 shows even higher magnifications on the specific spots in the structures. Two kinds of dendrites of the as-SLMed IN718 alloys on vertical section (X–Z plane) were observed at the E_vs of (a) 85.86 J/mm^3, (b) 100 J/mm^3, and (c) 117.17 J/mm^3. At a lower E_v, cellular dendrites with clear boundaries are formed, and the grains are distributed at a certain angle, as evidenced in Figure 8a,d. At the E_v level of 100 J/mm^3, the dendrites' arrays are refined (Figure 8b), and the directional solidified slender columnar constructures with visible boundaries are observed, as shown in Figure 8e. At a high E_v, there is no obvious cellular dendrite formed, but large-area particle agglomeration occurs. The coarsened and large columnar dendrites are distributed directionally with a fragmentized characteristic. Disconnected dendrite constructures with incomplete precipitants at the interdendritic region were exhibited. It is difficult to distinguish a single dendrite due to its clustering during the fast solidification process in the molten pool, as shown in Figure 8c,f. The primary columnar dendrites are dispersed at an increased volume energy density, despite the columnar dendrites being irregularly arranged.

3.3. Microhardness Distribution

Figure 9 shows the microhardness distribution and average microhardness of different energy densities measured on the polished sections of as-SLMed parts from bottom to top. Upon increasing the E_v from 85 J/mm^3 to 100 J/mm^3, the average microhardness increased from 266.13 $HV_{0.1}$ to 300.13 $HV_{0.1}$. This result was mainly due to the appearance of tiny pores at lower energy densities, which tend to expand the size and number of pores under load during the Vickers hardness test. Moreover, the samples with different energy densities have different standard deviations on measurement, and microhardness measured by the different positions of the same sample generates a large change during the hardness test. This large distribution in hardness is caused by the inhomogeneous distribution of the microstructure [53]. The appearance of fine microstructure for the sample at the E_v of 100 J/mm^3 allows the γ matrix to acquire more Nb elements. It is worth noting that the morphology and concentration of the Laves phase were found to be the most critical factors in the microstructure of Inconel 718 alloy [54,55]. The Laves phase is the Nb-rich phase in the γ matrix (see Figures 7 and 8). Moreover, the addition of Nb promotes the formation of supersaturated solid solution and enhances the solid-phase strengthening effect. According to the above analysis, the microhardness of the present Inconel 718 parts was enhanced by densification behavior, grain refinement, precipitation strengthening, and solid-solution strengthening.

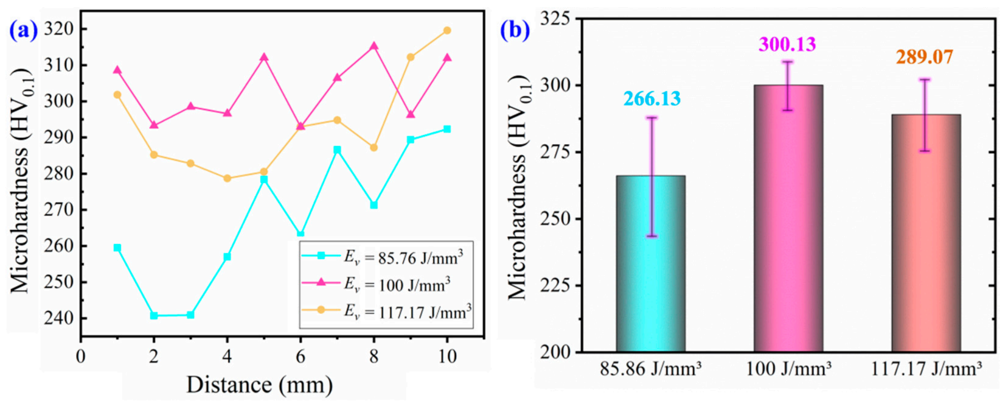

Figure 9. Vickers hardness in the X–Z plane of SLMed IN718 samples with different laser volume energy densities: (**a**) hardness distribution and (**b**) average hardness value.

4. Conclusions

Inconel 718 samples were fabricated by SLM with different process parameters. The effects of laser energy density on the relative density, microstructure, and microhardness of the as-SLMed Inconel 718 samples were analyzed. The following conclusions can be drawn:

1. The relative density firstly increased and then decreased slightly with the increase in the laser volume energy density. When the laser volume energy density was 100 J/mm^3, the material density reached a peak value of 99.53%.
2. When the laser energy density was 41.67 J/mm^3, the insufficient energy input resulted in poor melt pool fluidity and insufficient filling of the inter-particle voids, which resulted in the appearance of many discrete melt pools. The proper increase in E_v benefited the improvement of densification. However, an excessive value of laser energy density (117.17 J/mm^3) resulted in high thermal stress and elements' evaporation, causing the appearance of gas pores, which will damage the mechanical properties of the sample.
3. When the E_v rose from 85.86 J/mm^3 to 100 J/mm^3, the microhardness of the Inconel 718 alloy fabricated by the SLM process firstly increased from 266.13 $HV_{0.1}$ to 300.13 $HV_{0.1}$. When the E_v further increased to 117.17 J/mm^3, the microhardness showed a slight decrease to 289.07 $HV_{0.1}$. The fluctuation of the microhardness was related to the densification degree, microstructure uniformity, and precipitation phase content of Inconel 718 alloy.

Author Contributions: Conceptualization, J.X. and Z.W.; methodology, J.N. and Y.S.; validation, Y.C. and C.L.; formal analysis, K.Y. and Y.C; investigation, J.X., Z.W. and Y.S.; resources, Y.C and Y.L.; data curation, J.X. and Z.W.; writing—original draft, J.X. and Z.W.; writing—review and editing, J.N., C.L. and Y.L.; supervision, K.Y. and Y.C; project administration, Y.L.; funding acquisition, Y.S., C.L. and Y.L. All authors have read and agreed to the published version of the manuscript.

Funding: The work was supported by the Key Research and Development Program of Hunan Province of China (2022GK2043), the National Natural Science Foundation of China (52105334), the Natural Science Foundation of Hunan Province of China (2021JJ40206, 2022JJ20025), and the Educational Commission of Hunan Province of China (21B0472).

Institutional Review Board Statement: Not applicable.

Informed Consent Statement: Not applicable.

Data Availability Statement: The data presented in this study are available on request from the corresponding author.

Conflicts of Interest: The authors declare no conflict of interest.

References

1. Zhang, Y.; Yu, J.; Lin, X.; Guo, P.; Yu, X.; Zhang, S.; Liu, J.; Huang, W. Passive Behavior of Laser Directed Energy Deposited Inconel 718 after Homogenization and Aging Heat Treatment. *Corros. Sci.* **2022**, *205*, 110439. [CrossRef]
2. Rai, A.K.; Paul, C.P.; Mishra, G.K.; Singh, R.; Rai, S.K.; Bindra, K.S. Study of Microstructure and Wear Properties of Laser Borided Inconel 718. *J. Mater. Process. Technol.* **2021**, *298*, 117298. [CrossRef]
3. Ji, H.; Song, Q.; Wang, R.; Cai, W.; Liu, Z. Evaluation and Prediction of Pore Effects on Single-Crystal Mechanical and Damage Properties of Selective Laser Melted Inconel-718. *Mater. Des.* **2022**, *219*, 110807. [CrossRef]
4. Yoo, J.; Kim, S.; Jo, M.C.; Park, H.; Jung, J.E.; Do, J.; Yun, D.W.; Kim, I.S.; Choi, B.G. Investigation of Hydrogen Embrittlement Properties of Ni-Based Alloy 718 Fabricated via Laser Powder Bed Fusion. *Int. J. Hydrogen Energy* **2022**, *47*, 18892–18910. [CrossRef]
5. Blakey-Milner, B.; Gradl, P.; Snedden, G.; Brooks, M.; Pitot, J.; Lopez, E.; Leary, M.; Berto, F.; du Plessis, A. Metal Additive Manufacturing in Aerospace: A Review. *Mater. Des.* **2021**, *209*, 110008. [CrossRef]
6. Shao, S.; Khonsari, M.M.; Guo, S.; Meng, W.J.; Li, N. Overview: Additive Manufacturing Enabled Accelerated Design of Ni-Based Alloys for Improved Fatigue Life. *Addit. Manuf.* **2019**, *29*, 100779. [CrossRef]
7. Sreeramagiri, P.; Bhagavatam, A.; Ramakrishnan, A.; Alrehaili, H.; Dinda, G.P. Design and Development of a High-Performance Ni-Based Superalloy WSU 150 for Additive Manufacturing. *J. Mater. Sci. Technol.* **2020**, *47*, 20–28. [CrossRef]
8. Zhang, S.; Wang, L.; Lin, X.; Yang, H.; Huang, W. The Formation and Dissolution Mechanisms of Laves Phase in Inconel 718 Fabricated by Selective Laser Melting Compared to Directed Energy Deposition and Cast. *Compos. Part B Eng.* **2022**, *239*, 109994. [CrossRef]
9. De Bartolomeis, A.; Newman, S.T.; Jawahir, I.S.; Biermann, D.; Shokrani, A. Future Research Directions in the Machining of Inconel 718. *J. Mater. Process. Technol.* **2021**, *297*, 117260. [CrossRef]
10. Sugihara, T.; Enomoto, T. High Speed Machining of Inconel 718 Focusing on Tool Surface Topography of CBN Tool. *Procedia Manuf.* **2015**, *1*, 675–682. [CrossRef]
11. Umbrello, D. Investigation of Surface Integrity in Dry Machining of Inconel 718. *Int. J. Adv. Manuf. Technol.* **2013**, *69*, 2183–2190. [CrossRef]
12. Zheng, Y.; Liu, F.; Zhang, W.; Liu, F.; Huang, C.; Gao, J.; Li, Q. The Microstructure Evolution and Precipitation Behavior of TiB2/Inconel 718 Composites Manufactured by Selective Laser Melting. *J. Manuf. Process.* **2022**, *79*, 510–519. [CrossRef]
13. Vrancken, B.; Thijs, L.; Kruth, J.P.; Van Humbeeck, J. Heat Treatment of Ti6Al4V Produced by Selective Laser Melting: Microstructure and Mechanical Properties. *J. Alloys Compd.* **2012**, *541*, 177–185. [CrossRef]
14. Chen, L.Y.; Liang, S.X.; Liu, Y.; Zhang, L.C. Additive Manufacturing of Metallic Lattice Structures: Unconstrained Design, Accurate Fabrication, Fascinated Performances, and Challenges. *Mater. Sci. Eng. R Rep.* **2021**, *146*, 100648. [CrossRef]
15. Zhu, G.; Pan, W.; Wang, R.; Wang, D.; Shu, D.; Zhang, L.; Dong, A.; Sun, B. Microstructures and Mechanical Properties of GTD222 Superalloy Fabricated by Selective Laser Melting. *Mater. Sci. Eng. A* **2021**, *807*, 140668. [CrossRef]
16. Hosseini, E.; Popovich, V.A. A Review of Mechanical Properties of Additively Manufactured Inconel 718. *Addit. Manuf.* **2019**, *30*, 100877. [CrossRef]
17. Zhang, S.; Lin, X.; Wang, L.; Yu, X.; Hu, Y.; Yang, H.; Lei, L.; Huang, W. Strengthening Mechanisms in Selective Laser-Melted Inconel718 Superalloy. *Mater. Sci. Eng. A* **2021**, *812*, 141145. [CrossRef]
18. Sui, S.; Tan, H.; Chen, J.; Zhong, C.; Li, Z.; Fan, W.; Gasser, A.; Huang, W. The Influence of Laves Phases on the Room Temperature Tensile Properties of Inconel 718 Fabricated by Powder Feeding Laser Additive Manufacturing. *Acta Mater.* **2019**, *164*, 413–427. [CrossRef]
19. Amato, K.N.; Gaytan, S.M.; Murr, L.E.; Martinez, E.; Shindo, P.W.; Hernandez, J.; Collins, S.; Medina, F. Microstructures and Mechanical Behavior of Inconel 718 Fabricated by Selective Laser Melting. *Acta Mater.* **2012**, *60*, 2229–2239. [CrossRef]
20. Lv, J.; Luo, K.; Lu, H.; Wang, Z.; Liu, J.; Lu, J. Achieving High Strength and Ductility in Selective Laser Melting Ti-6Al-4V Alloy by Laser Shock Peening. *J. Alloys Compd.* **2022**, *899*, 163335. [CrossRef]

21. Yi, J.H.; Kang, J.W.; Wang, T.J.; Wang, X.; Hu, Y.Y.; Feng, T.; Feng, Y.L.; Wu, P.Y. Effect of Laser Energy Density on the Microstructure, Mechanical Properties, and Deformation of Inconel 718 Samples Fabricated by Selective Laser Melting. *J. Alloys Compd.* **2019**, *786*, 481–488. [CrossRef]
22. Pede, D.; Li, M.; Virovac, L.; Poleske, T.; Balle, F.; Mu, C. Microstructure and Corrosion Resistance of Novel β-Type Titanium Alloys Manufactured by Selective Laser Melting. *J. Mater. Res. Technol.* **2022**, *19*, 4598–4612. [CrossRef]
23. Riemer, A.; Leuders, S.; Thöne, M.; Richard, H.A.; Tröster, T.; Niendorf, T. On the Fatigue Crack Growth Behavior in 316L Stainless Steel Manufactured by Selective Laser Melting. *Eng. Fract. Mech.* **2014**, *120*, 15–25. [CrossRef]
24. Cruz, V.; Chao, Q.; Birbilis, N.; Fabijanic, D.; Hodgson, P.D.; Thomas, S. Electrochemical Studies on the Effect of Residual Stress on the Corrosion of 316L Manufactured by Selective Laser Melting. *Corros. Sci.* **2020**, *164*, 108314. [CrossRef]
25. Lu, Y.; Wu, S.; Gan, Y.; Huang, T.; Yang, C.; Junjie, L.; Lin, J. Study on the Microstructure, Mechanical Property and Residual Stress of SLM Inconel-718 Alloy Manufactured by Differing Island Scanning Strategy. *Opt. Laser Technol.* **2015**, *75*, 197–206. [CrossRef]
26. Ivanov, D.; Travyanov, A.; Petrovskiy, P.; Cheverikin, V.; Alekseeva, E.; Khvan, A.; Logachev, I. Evolution of Structure and Properties of the Nickel-Based Alloy EP718 after the SLM Growth and after Different Types of Heat and Mechanical Treatment. *Addit. Manuf.* **2017**, *18*, 269–275. [CrossRef]
27. Wang, L.-Z.; Wang, S.; Wu, J.-J. Experimental Investigation on Densification Behavior and Surface Roughness of AlSi10Mg Powders Produced by Selective Laser Melting. *Opt. Laser Technol.* **2017**, *96*, 88–96. [CrossRef]
28. Wen, Z.; Song, X.; Chen, D.; Fan, T.; Liu, Y.; Cai, Q. Electrospinning Preparation and Microstructure Characterization of Homogeneous Diphasic Mullite Ceramic Nanofibers. *Ceram. Int.* **2020**, *46*, 12172–12179. [CrossRef]
29. Song, X.; Zhang, K.; Song, Y.; Duan, Z.; Liu, Q.; Liu, Y. Morphology, Microstructure and Mechanical Properties of Electrospun Alumina Nanofibers Prepared Using Different Polymer Templates: A Comparative Study. *J. Alloys Compd.* **2020**, *829*, 154502. [CrossRef]
30. Wang, R.; Chen, C.; Liu, M.; Zhao, R.; Xu, S.; Hu, T.; Shuai, S.; Liao, H.; Ke, L.; Vanmeensel, K.; et al. Effects of Laser Scanning Speed and Building Direction on the Microstructure and Mechanical Properties of Selective Laser Melted Inconel 718 Superalloy. *Mater. Today Commun.* **2022**, *30*, 103095. [CrossRef]
31. Pan, H.; Dahmen, T.; Bayat, M.; Lin, K.; Zhang, X. Independent Effects of Laser Power and Scanning Speed on IN718's Precipitation and Mechanical Properties Produced by LBPF plus Heat Treatment. *Mater. Sci. Eng. A* **2022**, *849*, 143530. [CrossRef]
32. Liu, X.B.; Xiao, H.; Xiao, W.J.; Song, L.J. Microstructure and Crystallographic Texture of Laser Additive Manufactured Nickel-Based Superalloys with Different Scanning Strategies. *Crystals* **2021**, *11*, 591. [CrossRef]
33. Ravichander, B.B.; Mamidi, K.; Rajendran, V.; Farhang, B.; Ganesh-Ram, A.; Hanumantha, M.; Shayesteh Moghaddam, N.; Amerinatanzi, A. Experimental Investigation of Laser Scan Strategy on the Microstructure and Properties of Inconel 718 Parts Fabricated by Laser Powder Bed Fusion. *Mater. Charact.* **2022**, *186*, 111765. [CrossRef]
34. Wang, W.; Wang, S.; Zhang, X.; Chen, F.; Xu, Y.; Tian, Y. Process Parameter Optimization for Selective Laser Melting of Inconel 718 Superalloy and the Effects of Subsequent Heat Treatment on the Microstructural Evolution and Mechanical Properties. *J. Manuf. Process.* **2021**, *64*, 530–543. [CrossRef]
35. Zhu, L.; Xu, Z.F.; Liu, P.; Gu, Y.F. Effect of Processing Parameters on Microstructure of Laser Solid Forming Inconel 718 Superalloy. *Opt. Laser Technol.* **2018**, *98*, 409–415. [CrossRef]
36. Liu, H.; Guo, K.; Sun, J.; Shi, H. Effect of Nb Addition on the Microstructure and Mechanical Properties of Inconel 718 Fabricated by Laser Directed Energy Deposition. *Mater. Charact.* **2022**, *183*, 111601. [CrossRef]
37. Chen, Y.; Guo, Y.; Xu, M.; Ma, C.; Zhang, Q.; Wang, L.; Yao, J.; Li, Z. Study on the Element Segregation and Laves Phase Formation in the Laser Metal Deposited IN718 Superalloy by Flat Top Laser and Gaussian Distribution Laser. *Mater. Sci. Eng. A* **2019**, *754*, 339–347. [CrossRef]
38. Kim, H.; Cong, W.; Zhang, H.C.; Liu, Z. Laser Engineered Net Shaping of Nickel-Based Superalloy Inconel 718 Powders onto Aisi 4140 Alloy Steel Substrates: Interface Bond and Fracture Failure Mechanism. *Materials* **2017**, *10*, 341. [CrossRef]
39. Ma, M.; Wang, Z.; Zeng, X. Effect of Energy Input on Microstructural Evolution of Direct Laser Fabricated IN718 Alloy. *Mater. Charact.* **2015**, *106*, 420–427. [CrossRef]
40. McLouth, T.D.; Witkin, D.B.; Bean, G.E.; Sitzman, S.D.; Adams, P.M.; Lohser, J.R.; Yang, J.M.; Zaldivar, R.J. Variations in Ambient and Elevated Temperature Mechanical Behavior of IN718 Manufactured by Selective Laser Melting via Process Parameter Control. *Mater. Sci. Eng. A* **2020**, *780*, 139184. [CrossRef]
41. Moussaoui, K.; Rubio, W.; Mousseigne, M.; Sultan, T.; Rezai, F. Effects of Selective Laser Melting Additive Manufacturing Parameters of Inconel 718 on Porosity, Microstructure and Mechanical Properties. *Mater. Sci. Eng. A* **2018**, *735*, 182–190. [CrossRef]
42. Liu, Y.; Liu, C.; Liu, W.; Ma, Y.; Tang, S.; Liang, C.; Cai, Q.; Zhang, C. Optimization of Parameters in Laser Powder Deposition AlSi10Mg Alloy Using Taguchi Method. *Opt. Laser Technol.* **2019**, *111*, 470–480. [CrossRef]
43. Liu, Y.; Liu, C.; Liu, W.; Ma, Y.; Zhang, C.; Liang, C.; Cai, Q. Laser Powder Deposition Parametric Optimization and Property Development for Ti-6Al-4V Alloy. *J. Mater. Eng. Perform.* **2018**, *27*, 5613–5621. [CrossRef]
44. Kladovasilakis, N.; Charalampous, P.; Tsongas, K.; Kostavelis, I.; Tzovaras, D.; Tzetzis, D. Influence of Selective Laser Melting Additive Manufacturing Parameters in Inconel 718 Superalloy. *Materials* **2022**, *15*, 1362. [CrossRef] [PubMed]
45. Su, C.H.; Rodgers, K.; Chen, P.; Rabenberg, E.; Gorti, S. Design, Processing, and Assessment of Additive Manufacturing by Laser Powder Bed Fusion: A Case Study on INCONEL 718 Alloy. *J. Alloys Compd.* **2022**, *902*, 163735. [CrossRef]
46. Liu, F.; Lin, X.; Leng, H.; Cao, J.; Liu, Q.; Huang, C.; Huang, W. Microstructural Changes in a Laser Solid Forming Inconel 718 Superalloy Thin Wall in the Deposition Direction. *Opt. Laser Technol.* **2013**, *45*, 330–335. [CrossRef]

47. Wang, H.; Wang, L.; Cui, R.; Wang, B.; Luo, L.; Su, Y. Differences in Microstructure and Nano-Hardness of Selective Laser Melted Inconel 718 Single Tracks under Various Melting Modes of Molten Pool. *J. Mater. Res. Technol.* **2020**, *9*, 10401–10410. [CrossRef]
48. King, W.E.; Barth, H.D.; Castillo, V.M.; Gallegos, G.F.; Gibbs, J.W.; Hahn, D.E.; Kamath, C.; Rubenchik, A.M. Observation of Keyhole-Mode Laser Melting in Laser Powder-Bed Fusion Additive Manufacturing. *J. Mater. Process. Technol.* **2014**, *214*, 2915–2925. [CrossRef]
49. Wang, L.; Cui, R.; Li, B.-Q.; Jia, X.; Yao, L.-H.; Su, Y.-Q.; Guo, J.-J.; Liu, T. Influence of Laser Parameters on Segregation of Nb during Selective Laser Melting of Inconel 718. *China Foundry* **2021**, *18*, 379–388. [CrossRef]
50. Wan, H.Y.; Zhou, Z.J.; Li, C.P.; Chen, G.F.; Zhang, G.P. Effect of Scanning Strategy on Grain Structure and Crystallographic Texture of Inconel 718 Processed by Selective Laser Melting. *J. Mater. Sci. Technol.* **2018**, *34*, 1799–1804. [CrossRef]
51. Deng, D.; Peng, R.L.; Brodin, H.; Moverare, J. Microstructure and Mechanical Properties of Inconel 718 Produced by Selective Laser Melting: Sample Orientation Dependence and Effects of Post Heat Treatments. *Mater. Sci. Eng. A* **2018**, *713*, 294–306. [CrossRef]
52. Parimi, L.L.; Ravi, G.; Clark, D.; Attallah, M.M. Microstructural and Texture Development in Direct Laser Fabricated IN718. *Mater. Charact.* **2014**, *89*, 102–111. [CrossRef]
53. Choi, J.P.; Shin, G.H.; Yang, S.; Yang, D.Y.; Lee, J.S.; Brochu, M.; Yu, J.H. Densification and Microstructural Investigation of Inconel 718 Parts Fabricated by Selective Laser Melting. *Powder Technol.* **2017**, *310*, 60–66. [CrossRef]
54. Olakanmi, E.O. Selective Laser Sintering/Melting (SLS/SLM) of Pure Al, Al-Mg, and Al-Si Powders: Effect of Processing Conditions and Powder Properties. *J. Mater. Process. Technol.* **2013**, *213*, 1387–1405. [CrossRef]
55. Park, J.H.; Bang, G.B.; Lee, K.A.; Son, Y.; Kim, W.R.; Kim, H.G. Effect on Microstructural and Mechanical Properties of Inconel 718 Superalloy Fabricated by Selective Laser Melting with Rescanning by Low Energy Density. *J. Mater. Res. Technol.* **2021**, *10*, 785–796. [CrossRef]